Complex zoning in apatite from the Idaho batholith: A record of magma mixing and intracrystalline trace element diffusion

JEFFREY H. TEPPER,[1,*] AND SCOTT M. KUEHNER[2]

[1]Department of Physics, Astronomy, and Geosciences, Valdosta State University, Valdosta, Georgia 31698, U.S.A.
[2]Department of Geological Sciences, AJ-20, University of Washington, Seattle, Washington 98195, U.S.A.

ABSTRACT

Apatite crystals in a sample of biotite granodiorite from the Idaho batholith display complex chemical zoning, characterized by abrupt changes in REE+Y+Si content, more subtle variations in S, Na, La/Yb, and Mn contents, and petrographic evidence for multiple episodes of partial resorption. The zoning is attributed to changes in melt composition, resulting from magma mixing and differentiation, although the possibility that some rounded cores may be inherited cannot be disproved. High S contents in apatite cores and the presence of an included anhydrite grain indicate crystallization from an oxidized host magma. Divalent cations that occupy the apatite Ca sites (Sr, Mn, Fe) show evidence of having been redistributed between zones by intracrystalline diffusion, whereas cations that participate in coupled substitutions involving the tetrahedral site (Si, Y, REE, Na, S) were not readily redistributed. The main REE substitution in this case is $REE^{3+} + Si^{4+} \leftrightarrow Ca^{2+} + P^{5+}$, and REE diffusion is rate-limited by slow Si diffusion. However, exchange of LREE (e.g., $LaSm_{-1}$) on the Ca sites does not involve Si and proceeds more rapidly, resulting in homogenization of La/Sm between zones within individual crystals. Relative diffusion rates inferred from zoning profiles in this study are: Mn, Sr, Fe, and $LaSm_{-1}$ are faster than Na, S, and $LaYb_{-1}$, which are faster than Si. These data imply that REE patterns can be decoupled from REE abundances during diffusion, and that even apatite zones or cores that appear sharply bounded in backscattered electron images may not retain their original chemical or Sr-Nd isotopic traits.

INTRODUCTION

Apatite is a common accessory phase in many igneous rocks, where it serves as an important host for a geochemically diverse group of trace elements including Sr, S, U, and the rare earth elements (REE). Apatite/melt partition coefficients for these elements are typically >1 (Watson and Green 1981; Sawka 1988), which makes apatite more sensitive to subtle changes in the concentrations of these elements during igneous processes than are the major rock-forming silicates (Bea et al. 1994; Boudreau et al. 1986; Gromet and Silver 1983). In addition to preserving magmatic history, experimental studies indicate that under some conditions apatite may survive anatexis, in which case inherited apatite cores could afford insights into the origins of crustally derived granites (Harrison and Watson 1984).

Despite its potential as a petrologic tool, there have been few studies of apatite zoning, perhaps because zoning within individual crystals is generally not visible in transmitted light. Knutson et al. (1985) reported luminescence zoning that correlated with U and REE concentrations in hydrothermal apatite crystals from a tin-tungsten deposit. On the basis of zoning profiles and the lack of chemical correlation among apatite

grains sampled on a meter scale, the zoning was attributed to heterogeneous fluid compositions. Patchy REE zoning and variable zoning among adjacent apatite crystals in a pegmatite have been described by Jolliff et al. (1989), who also attribute these features to disequilibrium crystallization in a heterogeneous melt/fluid system. Sectoral zoning in apatite grains from hydrothermal veins and pegmatites has been described by Rakovan and Reeder (1994). However, none of these studies provides detailed analysis of zoning features in magmatic apatite crystals, which is the focus of this paper.

In this study, we have used backscattered electron (BSE) imaging, electron microprobe analyses, and ion microprobe analyses to characterize zoning patterns in apatite crystals separated from a granodiorite. Because this sample was collected in an area where the granitoid rocks contain a significant component of inherited zircon (Shuster and Bickford 1985), one objective of this study is to evaluate the possibility that some apatite grains may also contain inherited cores. Trace-element zoning profiles in apatite also have important potential for investigating the time-temperature history of crustal melting events. Diffusion rates in apatite, unlike those in zircon, are rapid enough to produce discernible chemical gradients within the time scale of a melting episode (Cherniak and Ryerson 1991, 1993). Measurements of such trace-element gradients for two

*E-mail: jtepper@valdosta.edu

or more elements, or for the same element in two or more minerals, combined with knowledge of their governing Arrhenius relations for diffusion, would allow calculation of the temperature and duration of the melting event (Watson and Harrison 1984). Although apatite diffusion data are available for Sr, Sm, Dy, and Pb (Cherniak 1997; Cherniak et al. 1991; Cherniak and Ryerson 1991, 1993; Watson et al. 1985), this technique has yet to be applied to trace-element gradients in naturally occurring apatites. A second objective of this paper, therefore, is to use the trace-element gradients in these apatite grains to infer relative diffusion rates for Mn, Sr, REE, S, Na, and Si. The results of this study have implications for the interpretation of inherited cores and other igneous zoning features, as well as for the mechanisms of diffusion.

GEOLOGIC SETTING AND SAMPLE DESCRIPTION

The Idaho batholith is a composite calc-alkaline batholith of Cretaceous to Early Tertiary age that occupies much of central Idaho and a part of western Montana (Shuster and Bickford 1985). The apatite crystals examined in this study were separated from a biotite granodiorite (91MT-68) collected in northeastern Idaho (46°19'7" N, 115°35'52" W) near the western margin of the Bitterroot lobe of the batholith (Fig. 1). Granitic rocks in this area were emplaced into amphibolite-facies Proterozoic metasediments, locally containing sillimanite, and are thought not to have risen far from their source (Wiswall and Hyndman 1987). Widespread migmatite zones at wallrock contacts and gradational contacts between intrusive units point to crystallization at >10 km depth (Shuster and Bickford 1985), as does the presence of magmatic epidote in sample 91MT-68. Although our sample has not been dated, it is thought by Lewis et al. (1992) to be approximately the same age as samples collected ~16 km and ~45 km away, respectively, along the Lochsa River that have yielded zircon U-Pb dates of 71 ± 9 and 75 ± 5 Ma (Toth and Stacey 1992). During the Eocene, these mesozonal Cretaceous granitoids were intruded by epizonal granites, indicating that the area had been uplifted to near surface levels by that time (Lewis et al. 1992).

Granodiorite sample 91MT-68 is mildly peraluminous [mol. $Al_2O_3/(CaO+Na_2O+K_2O) = 1.06$], and has strongly fractionated REE ($La/Yb_N = 30$) and low levels of HREE ($Yb_N = 3.7$) and Y (Table 1). These characteristics are shared by other granites in the area (Shuster and Bickford 1985), which typically also have high initial $^{87}Sr/^{86}Sr$ values (Fleck and Criss 1985) and extensive inheritance among zircons (Mueller et al. 1995). Trace-element and isotopic systematics of the Cretaceous granitoids in this region of the batholith indicate that they formed by mixing of magmas derived from a heterogeneous, deep-crustal Proterozoic source that contained residual garnet and zircon (Shuster and Bickford 1985; Fleck 1990; Mueller et al. 1995).

Sample 91MT-68 is medium grained and hypidiomorphic, consisting predominantly of euhedral plagioclase (An_{29} $Ab_{70}Or_{01}$-$An_{24}Ab_{75}Or_{01}$), and anhedral grains of quartz, biotite, and alkali feldspar ($An_{01}Ab_{08}Or_{91}$-$An_{00}Ab_{05}Or_{95}$), the latter forming poikilitic patches up to 5 mm across and locally containing myrmekite. Biotite flakes (Table 2) are typically found between plagioclase euhedra in clusters of 2–6 grains. Apatite grains
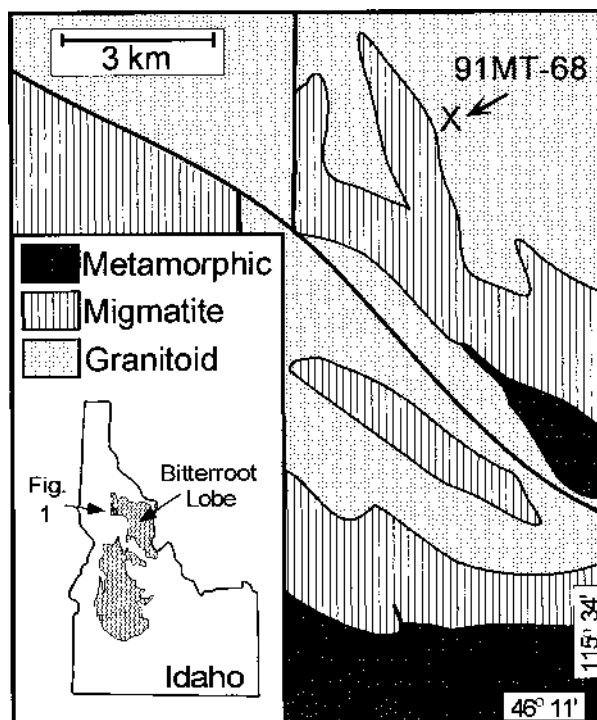

FIGURE 1. Simplified geologic map (after Lewis et al. 1992) showing the Idaho batholith (gray region in inset map) and the 91MT-

occur as stubby euhedra up to 1 mm in length and are scattered throughout the sample, although most commonly they are clustered with, or included within, biotite or quartz. Subhedral grains of allanite are typically enclosed within plagioclase or biotite and may reach 1 mm in length. Other accessory phases include

TABLE 1. Whole rock chemical and modal data

wt%		ppm				modal%	
SiO_2	70.97	V	44	La	33.9	plagioclase	41.8
TiO_2	0.34	Cr	32	Ce	66.5	quartz	40.6
Al_2O_3	14.82	Co	61	Pr	7.5	alkali feldspar	5.0
Fe_2O_3	2.89	Ni	18	Nd	26.5	biotite	10.3
MnO	0.05	Zn	42	Sm	4.61	apatite	0.13
MgO	1.22	Rb	76	Eu	1.05	allanite	0.07
CaO	2.65	Sr	679	Gd	3.39	white mica	0.87
Na_2O	3.92	Y	9	Tb	0.42	zircon	0.07
K_2O	2.50	Zr	186	Dy	1.98	myrmekite	1.0
P_2O_5	0.11	Nb	8.2	Ho	0.35		
Total	99.47	Cs	1.43	Er	0.85		
		Ba	1196	Tm	0.11		
S	<0.01	Hf	4.5	Yb	0.77		
		Ta	1.93	Lu	0.12		
		Th	7.7				
		U	1.3				

Note: Major elements determined by XRF at Stanford University (J. Sparks, analyst) with total Fe reported as Fe_2O_3; S determined by the LECO method at Chemex Labs. Trace elements analyzed in triplicate by ICP-MS at Union College, following lithium metaborate fusion of 0.1 g sample. Based on analyses of four natural standards, relative accuracy is estimated at <5% for all elements except Ni, Nb, Cs, Hf, Ta, Th, and U (<10%) and Cr and Zn (<20%). Relative precision, based on replicate analyses of samples and standards, is <5% for all elements except Cr, Zr, and U (<10%) and Ni (<15%). Modal data based on 1500 points counted.

TABLE 2. Representative biotite and anhydrite analyses

	matrix biotite (core)	matrix biotite (rim)	biotite inclusion (in F-7)	anhydrite inclusion (in F-7)
SiO_2	35.48	36.04	36.25	—
TiO_2	2.75	3.16	3.20	—
Al_2O_3	15.98	15.63	15.12	—
Fe_2O_3*	3.55	4.13	3.03	—
FeO†	16.80	16.80	16.80	—
MgO	9.95	9.96	10.74	—
MnO	0.39	0.40	0.57	—
BaO	0.22	0.24	0.23	—
CaO	—	—	—	41.68
Na_2O	0.08	0.07	0.27	—
K_2O	9.89	9.91	9.59	—
F	0.54	0.55	0.46	—
Cl	0.00	0.01	0.00	—
H_2O‡	3.29	3.30	3.40	—
SO_3	—	—	—	57.35
O=F,Cl	−0.23	−0.23	-0.19	—
Total	98.96	99.93	99.50	99.03
X_{phlog}	0.39	0.38	0.42	—
X_{sider}	0.39	0.37	0.32	—
X_{annite}	0.22	0.25	0.26	—

Note: Biotite compositions reported as mole fractions of phlogopite, siderophyllite, and annite, calculated after Czamanske et al. (1981).
* Ferric iron determined by difference between microprobe Fe analysis and volumetric ferrous iron determination.
† Ferrous iron content was determined volumetrically on 0.1 g of biotite separated from the whole rock.
‡ H_2O calculated assuming (OH+F+Cl) = 2 per 22 anions.

zircon, rare monazite, very scarce pyrite largely replaced by hydrous iron oxides, and rare Fe-Ti oxides present as magnetite accompanied by minor exsolved ilmenite. Rare white micas up to 0.5 mm long located along feldspar grain boundaries or as partial replacement products of biotite are probably evidence of minor deuteric alteration. Similarly, some biotite grains display minor chloritization and/or undulatory extinction but these features are uncommon.

BSE images show that most of the magmatic phases are complexly zoned. Many plagioclase and alkali feldspar grains have mottled and resorbed cores and rhythmically zoned concentric rims. Allanite, apatite, and zircon grains display very complex zoning and the allanite grains are zoned outward to REE-poor compositions.

ANALYTICAL METHODS

Apatite grains were separated from several kilograms of fresh granodiorite using a Rogers table and a magnetic separator. Hand-picked crystals were then mounted in epoxy disks each containing 50–100 crystals of similar size. These disks were polished until the exposure was close to, or through, the core of each grain, and then examined with BSE imaging to identify grains with distinct zoning. In addition, a smaller number of crystals were analyzed in six polished thin sections where it was possible to examine relationships between apatite and adjacent minerals in the rock.

Electron microprobe analyses were obtained at the University of Washington with a four spectrometer JEOL 733 Superprobe. Various analytical conditions were evaluated to eliminate potential beam-induced element mobility and still permit precise determination of minor-element concentrations. No significant variations in count rates were observed on apatite standards during a 1200 s time period using a 15 kV accelerating voltage, 10 nA beam current, and 10 μm beam diameter. Calcium, phosphorus, and oxygen dominate the composition of these apatite crystals, with the minor elements accounting for 1.5 wt% or less of the total. Therefore, to minimize the beam exposure on the sample, background rates were not collected on the samples during analysis, but were fixed to rates obtained from the analysis of a natural apatite standard prior to each session. For trace-element analyses, peak intensities were counted simultaneously on two spectrometers for 600 s at each point and the resulting concentrations averaged. The counting error was calculated from the sum of the measured peak and

TABLE 3. Textural and chemical characteristics of apatite zones

Zone	Occurrence (% of 23 xls)		Textural features	Chemical characteristics (wt%)						
				SiO_2	Y_2O_3	$(La/Yb)_N$	Na_2O	SO_3	MnO	Sr
1	6	(26%)	medium brightness, appears rounded or truncated by zones 2 or 3, no oscillations	0.15 (4)	0.19 (5)	0.81 (32)	0.11 (1)	0.19 (7)	0.13 (3)	0.05 (1)
2	12	(52%)	medium brightness, coarse oscillations, generally appears rounded or embayed by zone 3	0.24 (10)	0.30 (10)	0.81 (26)	0.09 (1)	0.12 (2)	0.14 (2)	0.06 (1)
3	23	(100%)	lowest brightness, no oscillations, commonly rounded or embayed	0.06 (3)	0.15 (2)	0.61 (21)	0.09 (1)	0.11 (3)	0.13 (2)	0.05 (1)
4	11	(48%)	bright band within or at outer edge of zone 3, typically discontinuous	0.20 (5)	0.28 (6)	0.43 (16)	0.09 (1)	0.17 (6)	0.13 (2)	0.05 (1)
5	23	(100%)	medium brightness, delicate oscillations, euhedral outline	0.16 (4)	0.25 (2)	0.55 (16)	0.09 (1)	0.11 (3)	0.13 (2)	0.05 (1)
6	7	(30%)	discontinuous bright patches along the boundary between zones 5 and 7	0.40 (14)	0.49 (17)	n/a	0.08 (1)	0.11 (2)	0.12 (2)	0.06 (1)
7	16	(70%)	outermost rim, lacks oscillations	0.12 (5)	0.22 (6)	0.30 (—)	0.08 (1)	0.05 (3)	0.09 (2)	0.05 (2)

Note: Chemical characteristics are reported as averages, with standard deviation (in parentheses) expressed relative to last decimal place. n/a = not analyzed.
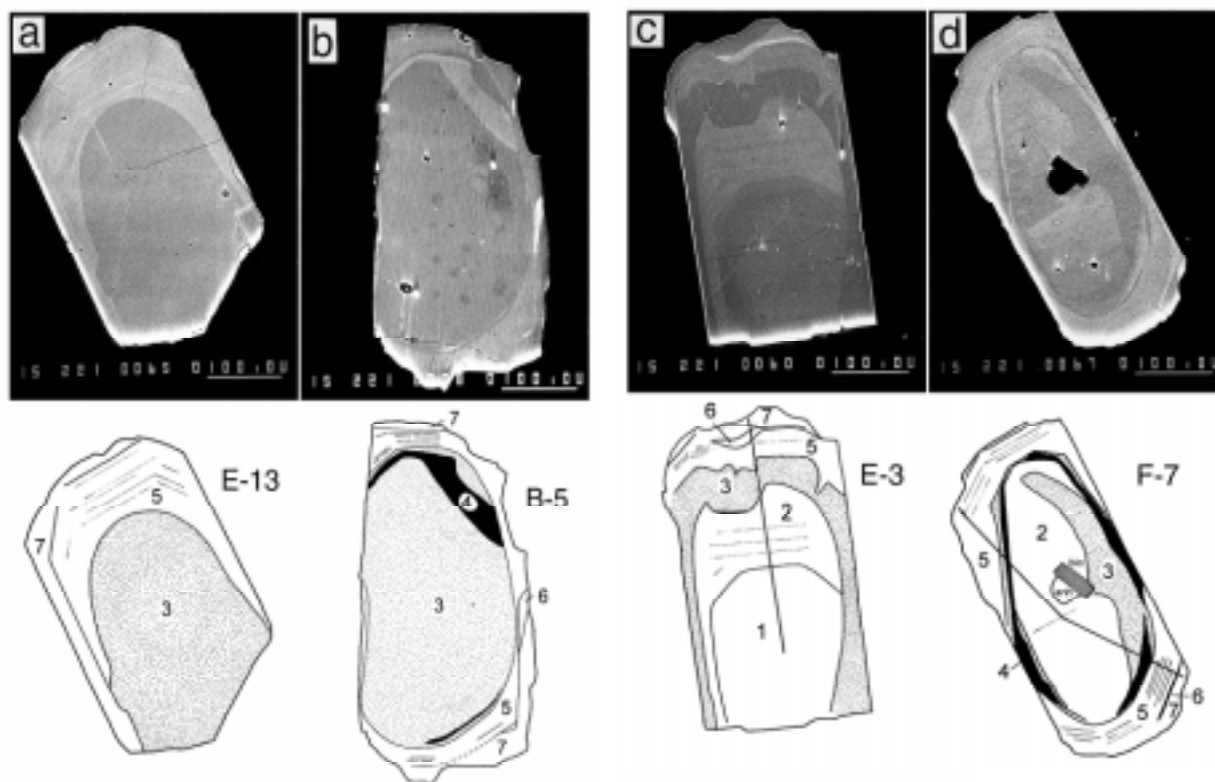
interpolated background intensities on both spectrometers. This method significantly reduces the minimum detection limits and counting error by doubling the effective peak counting time, but not at the expense of doubling the dwell time. To minimize potential beam damage, a maximum of four elements (two elements on each spectrometer pair) were acquired at each point along a line scan. The remainder of the minor elements were acquired during a second, parallel line scan approximately one beam diameter from the first. BSE images obtained after each line scan were used to locate precisely individual analysis points relative to one another and to zone boundaries. Matrix corrections for trace-element analyses were done offline using fixed Ca and P concentrations and the ZAF factors determined from full analyses of natural apatite standards.

REE contents were measured with a Cameca IMS-3f ion microprobe at Woods Hole Oceanographic Institute. These analyses used a primary beam of negatively charged oxygen ions with a current of 1–2 nA, which was focused to a diameter of 10–15 μm. Energy filtering of –60 eV was used to suppress molecular ion interferences. With Durango apatite as a standard, empirical relationships between secondary ion intensities and concentration (working curves) were determined and used to calculate REE concentrations (normalized to Ca). Analytical uncertainty, based on counting statistics, is generally less than 10%. Secondary electron images obtained after the analyses were acquired were used to locate the ion microprobe analysis points relative to zone boundaries. Ce concentrations determined by ion microprobe are generally lower than those determined by electron microprobe, although for most points
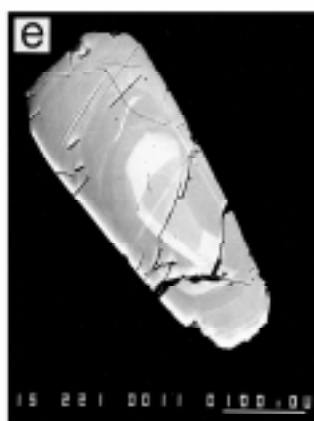
FIGURE 2. BSE images and line drawings of apatite crystals. Scale bar in each photograph is 100 μm long. Crystals are arranged from simplest (lacking early formed zones) to most complex; numbers in line drawings indicate zones. Labeled inclusions in (**d**) are biotite and anhydrite. Drawings **c**, **d**, and **e** include lines that show paths of electron microprobe traverses plotted in Figure 3.
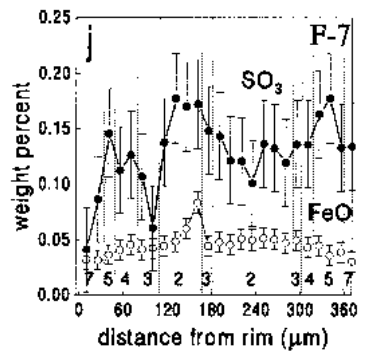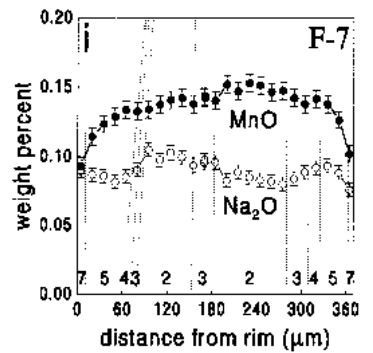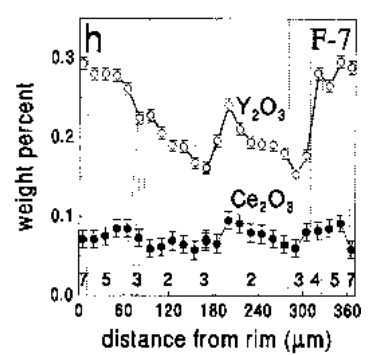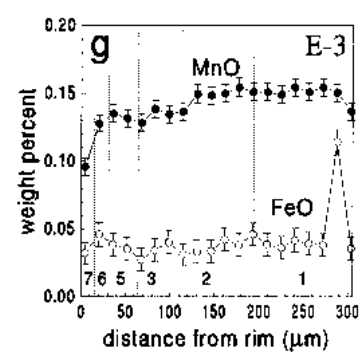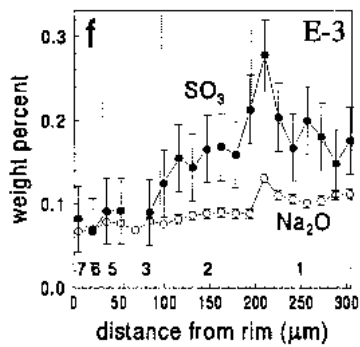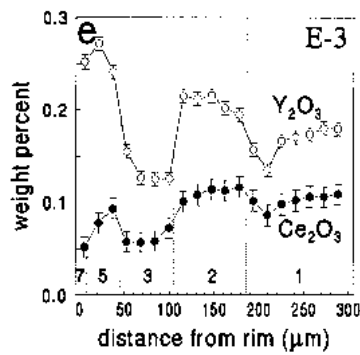
FIGURE 3. Trace element zoning profiles. Locations of traverses are indicated on line drawings in Figures 2c, 2d, and 2e. Vertical dotted lines indicate zone boundaries as located from BSE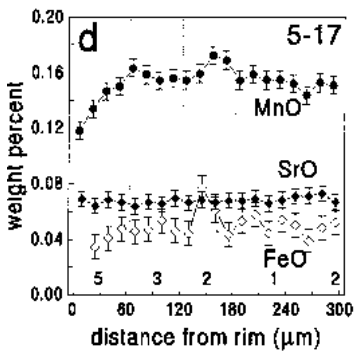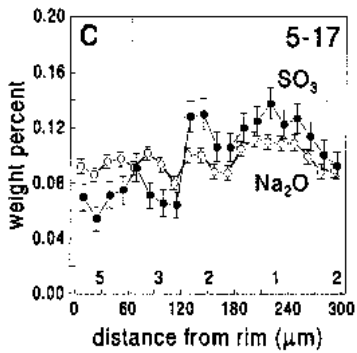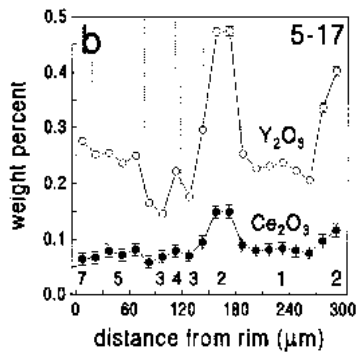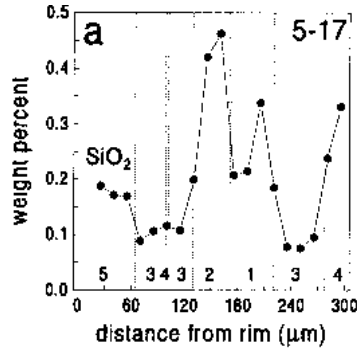 images; zone numbers are indicated at bottom of each plot. Error bars represent ±2σ analytical uncertainty based on counting statistics. In some cases this uncertainty is smaller than the data points and no error bars are visible.

TABLE 4. Representative apatite analyses

Apatite	5-17	E-3	5-17	E-3	F-7	5-17	E-3	F-7	B-5	E-13	D-4	5-17	F-7	B-5
Zone	1	1	2	2	2	3	3	3	3	3	3	4†	4	4
CaO	54.68	54.99	54.47	55.14	55.05	55.03	54.92	55.10	54.72	55.14	54.73	54.31	54.68	54.58
P_2O_5	41.08	41.02	41.19	41.06	41.07	42.17	41.71	41.41	41.29	41.26	40.71	41.49	41.51	41.71
F	3.16	3.31	3.10	3.26	3.20	3.33	3.29	3.12	3.14	3.24	3.56	3.25	3.20	3.07
Cl	0.01	0.02	0.00	0.05	0.00	0.01	0.01	0.00	0.00	0.00	0.00	0.01	0.00	0.00
SiO_2	0.21	0.12	0.44	0.16	0.16	0.09	0.03	0.03	0.05	0.06	0.03	0.12	0.21	0.18
Y_2O_3	0.23	0.17	0.47	0.21	0.20	0.15	0.13	0.17	0.11	0.15	0.15	0.22	0.20	0.27
Ce_2O_3	0.08	0.10	0.15	0.11	0.08	0.07	0.06	0.07	0.04	0.04	0.06	0.08	0.06	0.07
Na_2O	0.11	0.11	0.09	0.09	0.08	0.10	0.08	0.10	0.10	0.09	0.10	0.08	0.08	0.10
SO_3	0.13	0.19	0.12	0.16	0.13	0.07	0.09	0.11	0.09	0.12	0.12	—	0.13	0.13
MnO	0.16	0.15	0.17	0.15	0.15	0.16	0.13	0.14	0.11	0.14	0.11	0.16	0.14	0.13
FeO	0.05	0.04	0.07	0.04	0.05	0.05	0.03	0.04	0.02	0.05	0.03	0.05	0.06	0.03
SrO	0.07	0.06	0.07	0.06	0.06	0.07	0.06	0.07	0.04	0.06	0.03	—	0.06	0.05
La	190	210	290	230	140	100	110	90	50	80	70	—	—	90
Ce	710	820	1170	850	570	390	430	370	180	320	270	—	—	490
Nd	820	890	1380	960	830	440	470	480	280	400	370	—	—	790
Sm	350	350	620	350	340	200	190	230	150	180	180	—	—	340
Eu	35	35	52	36	28	22	18	22	16	19	20	—	—	33
Dy	510	310	930	360	430	270	240	300	230	280	280	—	—	460
Er	260	170	510	190	200	140	140	140	120	140	160	—	—	280
Yb	170	120	350	130	150	120	90	100	100	90	100	—	—	200

Note: Oxides determined by electron microprobe are reported in weight percent, with detection limits calculated after Ziebold (1967); REE determined by ion microprobe are reported in parts per million.
*Analysis point may have partially overlapped another zone or the edge of the grain.

(13 of 20) agreement between the two methods is within 20%. At the other seven points, concentrations of Ce measured with the ion microprobe are 30–50% lower than those obtained with the electron microprobe. However, REE patterns are not affected by the changes in Ce concentration, indicating that the other REE must vary sympathetically with Ce.

APATITE ZONING AND INCLUSIONS

BSE images of apatite grains separated from 91MT-68 reveal complex zoning that is not visible in transmitted light (Fig. 2). From a detailed study of twenty-three grains, seven zones were identified based on relative grayscale in BSE images, trace element concentrations, "stratigraphic" position within the crystal, and textural features such as evidence of resorption and the presence or absence of internal oscillations. The zones are designated 1 through 7 in order of decreasing stratigraphic age (Table 3). Individual zones can be correlated among grains and always occur in the same order, although only zones 3 and 5 are recognized in all apatite grains studied. Boundaries between zones are abrupt in BSE images, and commonly display an euhedral outline. In some cases, however, earlier zones appear to have been partially resorbed prior to growth of a later one (Fig. 2), producing rounded surfaces or embayments in the earlier zones. These textures are most widespread in the earliest-formed zones, with clear evidence of resorption in all examples of zones 1 and 2 (except in one grain where the BSE image is not clear), in at least two-thirds of the zone 3 examples, and in about half of the zone 4 examples. Conversely, zones 5 and 7 lack evidence of resorption in all studied grains. Zone 6, although discontinuous and irregular in outline, displays no obvious signs of resorption (e.g., no truncations or embayments). Oscillations are a feature of zones 2 and 5, but differ between the two zones. Those in zone 2 (Figs. 2c and 2d) are coarser, commonly >10 μm in width, less uniform in thickness and outline (not always parallel to major zone boundaries), and involve larger compositional changes (based on brightness contrasts in BSE images), whereas those in zone 5 (Figs. 2a, 2b, and 2d) appear uniform in width and <5 μm wide, are relatively straight (parallel to major zone boundaries), and involve a smaller compositional range.

Variations in brightness of BSE images correspond to differences in mean atomic number, which in these apatites result primarily from variations in REE + Y content. Concentrations of these elements are up to 9 times higher in the brightest zone (6) than in the darkest one (3) (Table 4). Although REE, Y, and Si concentrations can change abruptly between adjacent zones, within individual crystals there are no systematic trends in concentration along core-to-rim traverses or across individual zones (Fig. 3). Most apatites grains are LREE-depleted, with $(La/Yb)_N$ <1 in 27 of 30 zones analyzed (Figs. 4 and 5b). There is considerable grain-to-grain variation in this ratio, even when comparisons are made between equivalent zones, but in most cases there is a decrease in $(La/Yb)_N$ toward the rim (Fig. 5b). Sulfur and Na vary in tandem, with highest concentrations in zones 1, 2, and 4 (Fig. 3, Table 3). Grains that lack these S-enriched zones generally show little or no core-to-rim variation in Na or S. In contrast to the abrupt changes in REE content, variations in both S and Na appear to be gradational across at least some zones and/or zone boundaries (Fig. 3).

Among the other trace elements analyzed, Mn and Fe show slight zoning in some grains, whereas Sr, Cl, and F reveal no discernible trends in any of the apatites studied. Variations in Mn concentration are most evident in grains that contain zones 1 or 2, which have 5–10% higher MnO than the other zones (Table 3, Fig. 3). Furthermore, 10 of 15 apatite grains analyzed for Mn show a 25–35% decrease in MnO over the outermost ~60 μm (Fig. 3). This decrease generally does not correspond to any zone boundary visible in BSE images, and extends over distances that are too long for the trend to be an artifact of the analysis or sample preparation. Iron contents are low in all of these grains and generally show no zone-to-zone variation. However, four of the six grains analyzed for Fe display trends

TABLE 4—*Extended*

Apatite zone	D-4 4	5-17 5	E-3 5	F-7 5	B-5 5	E-13 5	D-4 5	E-3 6	B-5 6	B-5 7	5-17 7	E-3 7	F-7 7*	D-4 7*	Detection limits
CaO	54.56	55.01	55.37	54.98	54.23	55.21	54.71	54.66	53.21	54.16	—	54.75	—	54.51	
P$_2$O$_5$	40.48	40.74	40.91	41.81	42.01	41.39	40.52	41.03	41.21	40.52	—	41.40	—	39.84	
F	3.31	3.59	3.25	3.18	2.99	3.17	3.25	3.25	2.86	3.38	—	3.29	—	3.71	
Cl	0.00	0.02	0.02	0.00	0.00	0.00	0.00	0.01	0.01	0.00	—	0.01	—	0.01	
SiO$_2$	0.19	0.17	0.13	0.17	0.16	0.14	0.20	0.25	0.59	0.09	0.19	0.09	—	0.08	0.004
Y$_2$O$_3$	0.29	0.25	0.26	0.28	0.24	0.26	0.23	0.41	0.73	0.19	0.28	0.25	0.29	0.14	0.011
Ce$_2$O$_3$	0.07	0.08	0.09	0.08	0.07	0.06	0.07	0.11	0.12	0.05	0.06	0.05	0.06	0.05	0.021
Na$_2$O	0.09	0.09	0.08	0.09	0.10	0.09	0.08	0.07	0.08	0.08	0.09	0.07	0.08	0.08	0.006
SO$_3$	0.15	0.07	0.09	0.13	0.14	0.12	0.12	0.09	0.09	0.07	0.07	0.08	0.04	0.09	0.009
MnO	0.10	0.15	0.13	0.13	0.12	0.13	0.11	0.14	0.10	0.11	0.12	0.10	0.10	0.06	0.011
FeO	0.03	0.04	0.04	0.04	0.03	0.04	0.03	0.03	0.03	0.02	0.04	0.03	0.03	0.02	0.010
SrO	0.03	0.07	0.07	0.04	0.05	0.05	0.04	0.08	0.04	0.03	0.07	0.06	—	0.04	0.010
La	60	150	190	110	80	110	130	—	—	—	—	—	—		
Ce	340	620	690	460	330	430	520	—	—	—	—	—	—		
Nd	550	720	760	630	500	600	650	—	—	—	—	—	—		
Sm	330	310	350	320	270	310	330	—	—	—	—	—	—		
Eu	37	33	33	37	31	30	30	—	—	—	—	—	—		
Dy	590	460	400	550	400	440	510	—	—	—	—	—	—		
Er	320	220	260	290	240	220	250	—	—	—	—	—	—		
Yb	230	160	170	220	170	170	220	—	—	—	—	—	—		

toward lower concentrations near the rims (Fig. 3), similar to the trends observed for Mn.

Zircon is the most common inclusion in apatite, but monazite and one or more Th-rich minerals (possibly thorite) also have been recognized. Needles of iron oxide are distributed heterogeneously throughout many grains but do not appear to be restricted to any particular zone. These needles range up to 25 µm in length and appear oriented parallel to the apatite *c* axis, suggesting that they may have exsolved from the host apatite. We also interpret oriented needles of iron sulfide found in zone 1 of one crystal as exsolution features (Fig. 6). It is unknown whether exsolved sulfide needles are present in any other zone(s), because of the difficulties of detecting sulfur in these small needles that generally lie below the apatite surface. The core (zone 2) of apatite F-7 contains a 50 µm wide grain of anhydrite that crystallized against biotite (Fig. 2d). The apatite-anhydrite contact is rounded, suggesting resorption/reaction with the magma, but the anhydrite-biotite contact is planar and sharp. The biotite is similar in composition to magmatic biotite elsewhere in the rock but has slightly higher contents of MnO and Na$_2$O, which are both characteristic of apatite zones 1 and 2, and slightly higher amounts of the phlogopite and annite components (Table 2). Both the biotite and the anhydrite are considered early magmatic phases, based on their texture and on the composition of the biotite.

SUBSTITUTIONS

Trace element variations within apatite involve substitutions on the tetrahedral P site and on two distinct Ca sites. The larger Ca(1) site is coordinated by nine O atoms, whereas the smaller Ca(2) site is coordinated by six O atoms and one column cation (F, Cl, or OH). Substitutions of interest in this study are divided into: (1) simple substitutions that involve only the Ca sites; (2) coupled substitutions that involve only the Ca sites; and (3) coupled substitutions that involve both the tetrahedral and the Ca sites.

The principal cations involved in simple substitutions for Ca^{2+}

are Mn^{2+}, Sr^{2+}, and Fe^{2+}. Manganese cations occupy both Ca sites in apatite, but show a preference for the larger Ca(1) sites, whereas Sr is strongly ordered into the Ca(2) site (Hughes et al. 1991a). Maximum concentrations of these elements in 91MT-68 apatites (0.23 wt% MnO, 0.08 wt% SrO, 0.07 wt% FeO) are typical of apatite associated with granitic rocks (Gunow 1983).

The REE (and Y) also occupy Ca sites in apatite, with the LREE (La→Pr) preferring the Ca(2) site and the heavier REE preferring the Ca(1) site (Hughes et al. 1991b). Substitution of REE^{3+} for Ca^{2+} requires the involvement of an additional cation to maintain charge balance, which can be achieved by the substitutions REE^{3+} + Si^{4+} ↔ Ca^{2+} + P^{5+} and/or REE^{3+} + Na$^+$ ↔ 2 Ca^{2+} (Ronsbo 1989). Among apatites analyzed in the present study, charge neutrality is maintained by a combination of both substitutions. The REE + Si substitution can account for about 70% of the total REE contents in all zones except 3, which is dominated by the REE + Na substitution (~60% of total REE). This shift in substitution during growth of zone 3 may reflect a change in the alkalinity (Ronsbo 1989) and/or silica activity of the melt (Watson and Green 1981). Although both of these parameters are known to affect the apatite substitution mechanism, the exact dependency has not yet been determined experimentally. Total REE and Si contents of all zones are typical of apatite from granites, although Y contents (maximum 0.73 wt% Y$_2$O$_3$) are up to four times higher than the average reported by Gunow (1983).

Sulfur substitutes into the tetrahedral site as the S^{6+} ion, and the strong correlation between Na and S contents (Fig. 3) suggests that charge balance is maintained through the coupled substitution S^{6+} + Na$^+$ ↔ Ca^{2+} + P^{5+}. Consistent with this substitution is the lack of correlation between S and Si, indicating that the substitution S^{6+} + Si^{4+} ↔ 2 P^{5+} is insignificant in this case. On a plot of formula proportions (REE + Y + S) vs. (Si + Na), our data straddle the 1:1 correlation line suggesting that no important substitutions involving these elements were overlooked (Fig. 7).
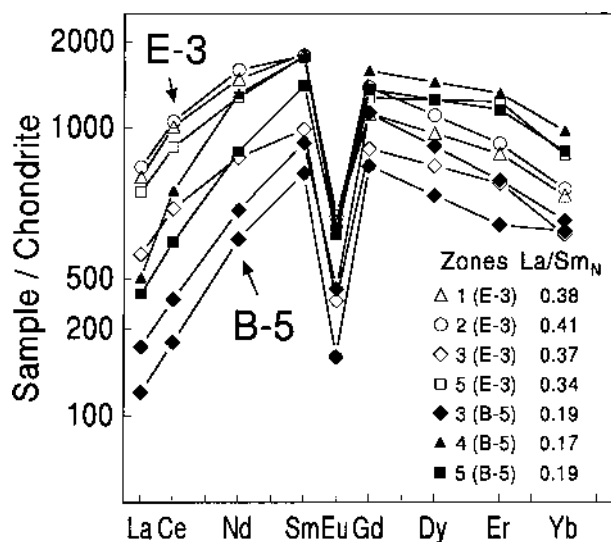
FIGURE 4. Chondrite-normalized REE data for individual zones in apatites E-3 and B-5 normalized to the recommended values of Boynton (1984). Gd values are interpolated; other data are in Table 4. Note that the crystals have overlapping HREE contents, but La contents and $(La/Sm)_N$ values of all zones in B-5 (which lacks zones 1 and 2) are lower than those of E-3 (which does contain zones 1 and 2).

POSSIBLE ORIGINS OF ZONING IN APATITE

Discontinuous compositional zoning in igneous minerals can result from several processes, including magma mixing, changes in crystal/melt element partitioning, inheritance, and kinetic effects. In this section we evaluate these four possible explanations for trace-element zoning in apatite from our sample of the Idaho batholith, focusing primarily on zoning in REE, Y, and Si as these elements are responsible for most of the observed compositional variations. Specific zoning features that must be explained include: (1) abrupt changes in composition that can be correlated among grains; (2) the lack of any systematic core to rim variations in element concentrations; and (3) evidence of multiple episodes of resorption.

Inheritance

Zircons from many granitic rocks of the northern Idaho batholith contain a significant component of inherited Pb (Shuster and Bickford 1985), and BSE images of zircon grains from sample 91MT-68 commonly reveal irregularly shaped cores that are probably inherited. This suggests the possibility that the early, rounded apatite zones (zones 1, 2, or 3) also may be inherited. One means of evaluating apatite inheritance is to apply the apatite solubility models of Harrison and Watson (1984) and Pichavant et al. (1992) to determine whether the whole rock P_2O_5 content of this sample (0.11 wt%) exceeds that required for apatite saturation at the temperature of magma formation. We have estimated the temperature at which the melt separated from its source using the zircon saturation of model of Watson and Harrison (1983) and the monazite saturation
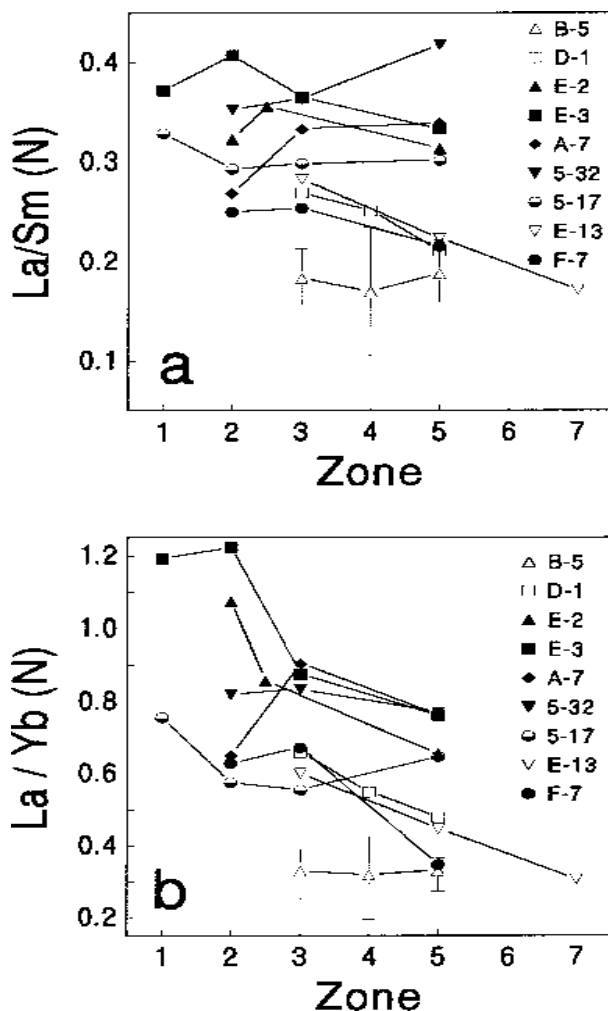

FIGURE 5. Intracrystalline variations in REE patterns. (a) $(La/Sm)_N$ data from nine apatite grains. Note the lack of systematic core-to-rim variation, and the fact that $(La/Sm)_N$ values are above 0.3 in most in grains that contain zones 1 and/or 2 (solid symbols), and below 0.3 in grains without these zones (open symbols). (b) $(La/Yb)_N$ values for the same apatite grains. Note that this ratio declines toward the rim in most cases, and that grains lacking zones 1 or 2 generally have lower $(La/Yb)_N$ in the other zones. Error bars for grain B-5 in both figures

model of Montel (1993). The former yields an average temperature (T_{zir}) of 800 °C (range = 791–812 °C based on four analyses of 91MT-68 containing 167–211 ppm Zr). This temperature represents a maximum if some Zr is present in inherited zircon cores that did not crystallize from the host magma, but is in good agreement with a temperature of 822 °C calculated on the basis of monazite saturation (T_{mon}). Assuming that sample 91MT-68 represents a liquid composition, application of the Harrison and Watson (1984) apatite solubility model (HW) indicates that at 800 °C, the melt would achieve saturation at 0.028 wt% P_2O_5, implying that up to 75% of the apatite in the rock is inherited. However, Pichavant et al. (1992) have shown that the HW model underestimates apatite solubility in peraluminous systems, and
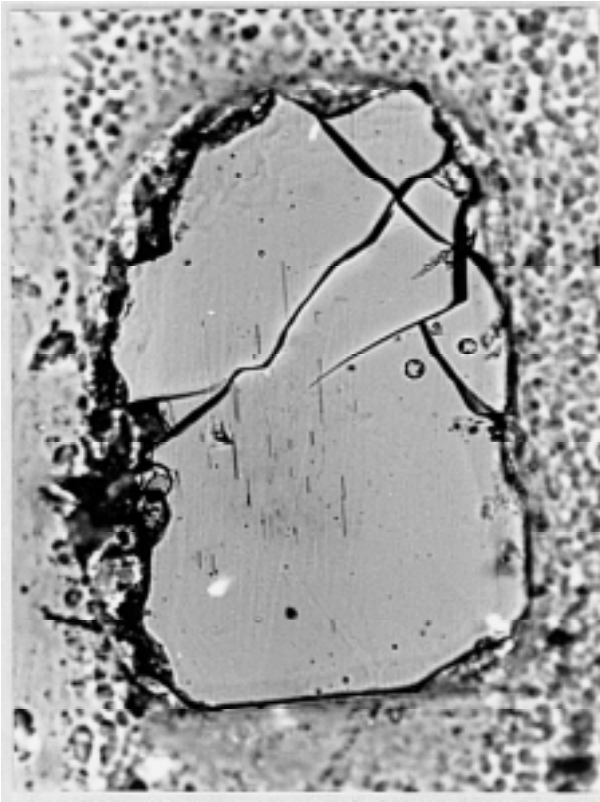
FIGURE 6. Oriented needles of iron sulfide (and iron oxide?) in the core of apatite C-7. These are interpreted as an exsolution feature, and in this case appear to be restricted to zone 1 (not visible in transmitted light). Transmitted light; length of crystal is approximately 220 μm.
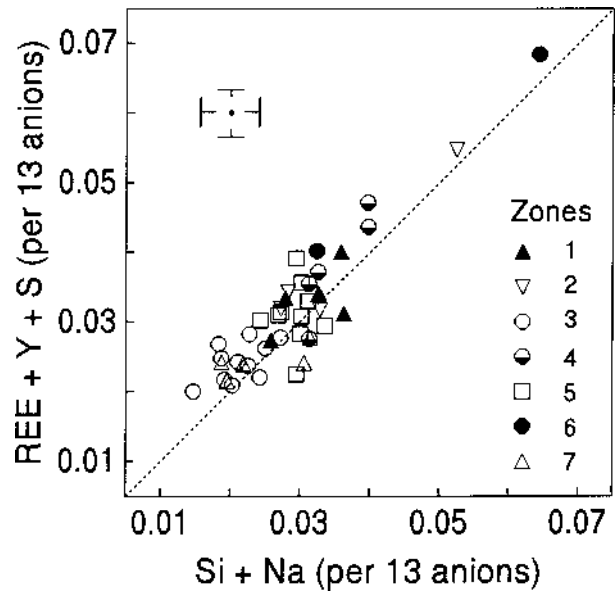

FIGURE 7. Plot showing good correlation between formula proportions of REE+Y+S and Si+Na. Each point represents an average of multiple analyses of a given zone for an individual apatite grain. Error bars indicate typical 2σ uncertainty calculated from 3 analyses of zone 3 in grain 5-17.

they proposed an extension to the HW model for application to peraluminous rocks. When applied to 91MT-68, the Pichavant et al. (1992) model (PMR) predicts apatite saturation at 640 °C (0.308 wt% P_2O_5 required for saturation at 800 °C). Although not impossible for an H_2O-rich granitic magma, this temperature is substantially below T_{zir} and T_{mon}, implying that all apatite grains in 91MT-68 crystallized late and that there are no inherited cores. Pichavant et al. (1992) note, however, that their model significantly overestimates apatite solubility for some samples, particularly those that contain >1.5 wt% Fe_2O_3 (as 91MT-68 does). Apatite solubility estimated for this sample on the basis of its alumina saturation index (Wolf and London 1994) is 0.055 wt% P_2O_5. This result is far below the PMR prediction, and roughly twice that of the HW model, but cannot be used to infer a saturation temperature. It is likely that the actual apatite saturation temperature for this sample lies somewhere between those predicted by the HW and PMR models, a temperature range that, unfortunately, sheds little light on the possibility of apatite inheritance.

Trace element evidence for inherited apatite cores is also equivocal. If some cores were inherited, one might expect to see sharp chemical discontinuities between these cores and the magmatic rims. However, many trace elements show no systematic differences between the early formed "cores" (zones

1–3) and the later-formed zones (4–7), although this lack of variation could result in part from intracrystalline diffusion (see below). $(La/Yb)_N$ ratios and S concentrations are generally higher in zones 1 and 2 than in the later zones, but these differences can be attributed to magmatic differentiation involving crystallization of monazite, allanite, and pyrite. For example, 60% crystallization of an assemblage containing only 0.0005 wt% monazite and 0.05 wt% each of allanite and zircon (the approximate modal proportions of these minerals) would be sufficient to produce the observed decrease in $(La/Yb)_N$ between zones 1 and 7 [based on partition coefficient data from Bea et al. (1994) and Mahood and Hildreth (1983)]. The fact that even early formed zones have relatively low $(La/Yb)_N$ (mostly <1) further suggests that apatite saturation occurred after the melt had been depleted in LREE by crystallization of monazite (which occurs as inclusions in apatite) and/or allanite (which formed early but has not been observed as an inclusion in apatite). Crystallization of early formed apatite zones after monazite and/or allanite would preclude apatite inheritance, unless the LREE-rich accessory phases are themselves inherited, in which case the melt phase was never LREE-enriched and apatite inheritance is permitted but not required. In summary, although the resorption features in zones 1–3 suggest that they could be inherited, there are no compositional features of these zones that preclude their being early formed crystals that precipitated from the host magma.

Kinetic effects

Factors influencing the incorporation of trace elements into a growing crystal include element diffusion rates in the melt, crystal

growth rates, and the kinetics of processes occurring at the crystal/melt interface. In situations where the rate of crystal growth exceeds the rate at which elements in the melt diffuse toward (or away from) the crystal-liquid interface, a compositional boundary layer may develop, enriched in incompatible elements and depleted in compatible elements (Bacon 1989; Kuehner and Joswiak 1995). Intermittent transfer of a growing apatite crystal between such a layer (for example, a REE-enriched boundary layer around a feldspar) and the bulk magma could produce discontinuous zoning, and even resorption if the boundary layer was apatite saturated but the bulk melt was not. However, this is an unlikely explanation for the zoning in our apatite grains for several reasons. First, development of a compositional boundary layer wide enough (>100 μm) to surround a growing apatite completely would require a rapid crystal growth rate. This is unlikely under the slow-cooling conditions associated with mesozonal intrusions (Bacon 1989). Second, most apatite grains in 91MT-68 are euhedral to subhedral and interstitial. Conversely, apatite crystals in volcanic rocks that are inferred to have grown in boundary layers around other minerals tend to be acicular and included within or attached to other host minerals (Bacon 1989). Third, there is no indication in thin section that apatite zoning is influenced by nearby phases; grains adjacent to allanite do not differ in zoning from those adjacent to feldspar or biotite. Fourth, a process that generates small-scale, local heterogeneities would probably not produce a coherent zoning stratigraphy that can be correlated between crystals.

In addition to boundary layers around major rock-forming minerals, it is also important to consider the possibility of REE-depleted boundary layers around individual apatites, which can develop if growth rates are high and diffusion rates in the melt are slower for REE than for P (Fig. 4 in Bacon 1989). Delicate oscillatory zoning observed in zone 5 may indicate chemical gradients in the melt surrounding these crystals during slow growth (Allegre et al. 1981). For the major zoning features we observe, however, boundary layers around apatite grains seem an unlikely explanation because: (1) individual zones do not display a gradual decrease in REE content that would reflect progressive REE depletion of the boundary layer; (2) this process does not account for resorption; and (3) such local heterogeneities in melt composition are unlikely to produce a consistent stratigraphy.

Variations in crystal growth rate can also influence the effective (as opposed to equilibrium) partitioning of trace elements between crystal and melt (Kouchi et al. 1983). During rapid growth a crystal may incorporate cations adsorbed on its surface that under equilibrium conditions would be excluded (i.e., $D_{EFF} > D_{EQM}$ for incompatible elements). This may act to dilute the concentrations of trace elements that are nominally compatible (i.e., $D_{EFF} < D_{EQM}$ for compatible elements). Both effects will be more pronounced with higher growth rates, and can produce sector zoning within individual crystals if growth rates on non-equivalent faces are different. Such zoning has been described in sphene (Paterson and Stephens 1992) and apatite (Rakovan and Reeder 1994), but bears little resemblance to the quasi-concentric zoning observed in the apatite grains of this study. Growth rate changes also fail to account for resorption, and would require a mechanism for triggering significant changes in growth rate (both increases and decreases) during

crystallization of a deep-seated pluton. Attributing the REE zoning to changes in growth rate would imply that the zones with the lowest REE concentrations grew most rapidly, causing compatible elements to be diluted, and conversely that zones with the highest REE concentrations grew more slowly and thus represent a closer approach to equilibrium partitioning. However, agreement between experimentally determined apatite/melt REE partition coefficients (D_{EXP}) and apparent distribution coefficients ($D_{APP} = REE_{XL}/REE_{WR}$) is significantly better for REE-poor zones (e.g., 3) than for REE-rich zones (e.g., 2). In the case of Sm, for example, the average D_{APP} is 41 for zone 3 and 87 for zone 2, whereas the range for D_{EXP} is 18–38 (Watson and Green 1981). For many REE, D_{APP} is outside the range of experimentally determined values for both zones, perhaps because the whole-rock composition does not accurately represent the liquid composition from which individual apatite zones crystallized. However, the fact that agreement between D_{EXP} and D_{APP} is consistently worse for the REE-rich zones (which should provide the closest approach to equilibrium partitioning) argues that growth rate variations are not responsible for the major REE zoning features in these apatite crystals.

Co-precipitation of REE-rich phases

In addition to apatite, major hosts for REE in this granodiorite include allanite, monazite, and zircon. The common occurrence of these minerals as inclusions within other phases indicates that they appeared early in the crystallization history. The impact of monazite and allanite crystallization on the REE chemistry of the melt is clearly reflected in the apatite crystals by their low LREE contents (Fig. 4) and core-to-rim decreases in $(La/Yb)_N$ (Fig. 5b). However, the crystallization of accessory phases cannot account for the multiple abrupt changes in REE content, particularly the concentration increases that characterize the apatite zoning. Epidote rims on allanite grains suggest that REE concentrations in the melt decreased significantly during crystallization, but provide no evidence of a reaction relationship that would have returned REE to the melt. Similarly, zircon crystallization might decrease the concentrations of HREE in residual melt, but cannot explain abrupt discontinuities in REE concentration. No differences in zoning patterns are observed around zircon inclusions in apatite, or in apatite grains adjacent to allanite, indicating that the apatite zoning was not influenced by the proximity of other REE-rich accessory phases.

Magma mixing

Apatite and several other magmatic phases (allanite, plagioclase, alkali feldspar, and zircon) in this sample display features characteristic of phenocrysts in mixed volcanic rocks, including resorption textures, abrupt compositional breaks between zones, and a lack of systematic core-to-rim chemical variations (O'Brien et al. 1988; Sakuyama 1979). With regard to apatite zoning, movement of a growing crystal through melt domains of differing composition could also explain the decoupling of trace element variations between zones. For example, the shift in REE substitution mechanism in zone 3, and the fact that in zone 4 the REE and S increase together while in zone 6 the REE increase but S does not, are difficult to attribute to any of the zoning processes discussed above, but are

compatible with a heterogeneous magma mixing scenario. Furthermore, apatite solubility in felsic peraluminous melts increases markedly with the alumina saturation index (ASI), from ~0.1 wt% P_2O_5 at ASI = 1.0-1.1 to ~0.63 wt% P_2O_5 at ASI = 1.3 (Wolf and London 1994). An influx of melt that raised this parameter would thus promote dissolution of existing apatites. Such influxes would be expected in an environment of crustal melting and may account for the resorption textures in these apatite grains. We do not suggest that each zone represents a new influx of magma: some zones with similar traits (e.g., 2 and 4) may reflect transfer of the apatite out of, and then back into, the same chemically distinct volume of melt, whereas other zones may reflect hybrid mixtures of magmas in varying proportions. In addition, the decrease in element concentrations and absence of oscillations that characterize the outermost zone 7 probably reflect the rapidly changing composition of the late stage residual melt. For the major zoning features, however, the most plausible explanation appears to involve mixing of compositionally dissimilar magmas and subsequent circulation of the growing apatite crystals through these chemically distinct regions. This would be consistent with petrologic studies of the northern Idaho batholith that have emphasized the role of mixing to explain whole-rock data that define linear trends on trace element ratio plots and hyperbolic arrays on ϵ_{Nd}-ϵ_{Sr} diagrams (Fleck 1990). Plutons of the group represented by sample 91MT-68 are modeled by Fleck (1990) as mixtures of deep-seated crustal melts, perhaps derived from upper and lower Proterozoic crust.

SULFUR ZONING AND f_{O_2} CONSTRAINTS

Sulfur zoning in apatite, together with the distribution of sulfate and sulfide minerals in the rock, provides constraints on the S content and f_{O_2} history of the 91MT-68 magma. The core (zone 2) of apatite F-7 contains an inclusion of magmatic anhydrite (Fig. 2d). Anhydrite has not previously been reported in granitic rocks, but is increasingly recognized as a phenocryst in oxidized volcanic systems (Luhr et al. 1984; Bernard et al. 1991). Experimental studies (Carroll and Rutherford 1987; Luhr 1990) indicate that anhydrite requires an f_{O_2} at least 1 to 1.5 log units above the Ni-NiO buffer, and such conditions for the 91MT-68 magma are consistent with an estimate of f_{O_2} slightly above Ni-NiO obtained from the Fe^{3+} content of biotite (Wones and Eugster 1965). Maximum S contents of 91MT-68 apatites (0.32 wt% S) are associated with zone 1, and are comparable to those of apatite phenocrysts that coexist with anhydrite in pumice from El Chichon (0.26–0.33 wt%) and Mt. Pinatubo (avg. 0.3 wt%), where the original SO_3 contents of the melts have been estimated at 2.5 wt% and 0.22–0.62 wt% respectively (Baker and Rutherford 1996). By comparison, the whole rock S content of 91MT-68 (<0.01 wt% S) is low, which may indicate that the system has lost sulfur, although anhydrite saturation in a low-temperature silicic magma requires less than ~200 ppm S in the melt (Carroll and Rutherford 1987; Luhr 1990).

Sulfur contents of 91MT-68 apatites decline by an average of 40% between zones 1–3. This may reflect a decrease in S content of the melt caused by magma mixing, crystallization of a sulfide phase, or decreasing temperature (Baker and Rutherford
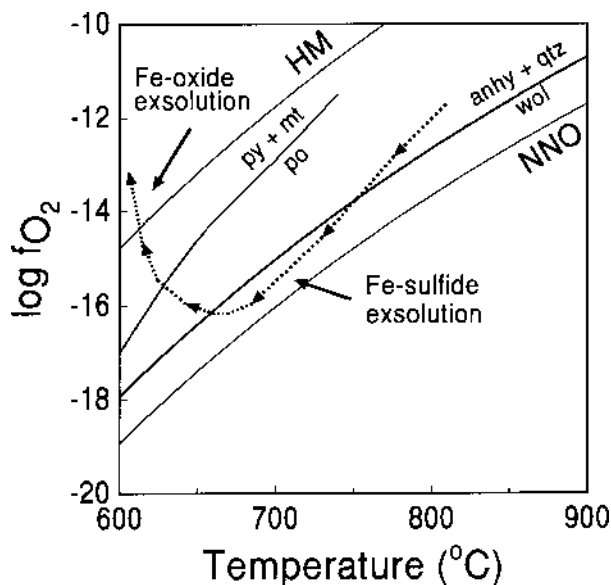

FIGURE 8. Plot of log f_{O_2} vs. temperature showing proposed path of 91MT-68 magma during cooling. Oxygen buffers calculated for 5 kb with equations from Frost (1991). Anhydrite stability limit taken from Carroll and Rutherford (1987). Exsolution of Fe-sulfide needles occurs when f_{O_2} drops below the SO_4^{2-}/S^{2-} equilibrium curve (taken as the anhy + qtz $\leftrightarrow$ wol boundary); subsequent exsolution of Fe-oxides occurs during subsolidus oxidation. See text for discussion.

1996). Decreasing f_{O_2}, with a concomitant drop in SO_4^{2-}/S^{2-} of the melt, may also play a role. The curve for the sulfate-sulfide reaction, $SO_4^{2-} \leftrightarrow S^{2-} + 2O_2$, has been determined experimentally to lie about 1 log unit above the NNO buffer and approximately parallel to it (Carroll and Rutherford 1987), although the T-f_{O_2} slope is not tightly constrained. Based on the stoichiometry of this reaction, the SO_4^{2-}/S^{2-} activity ratio of the melt should decrease by a factor of 100 for each log unit decrease in f_{O_2} below the equilibrium curve. Such f_{O_2} decreases could result from magma mixing, or could be a consequence of cooling along a T-f_{O_2} path that cuts across the SO_4^{2-}/S^{2-} isopleths (Fig. 8). The resulting decrease in SO_4^{2-}/S^{2-} of the melt would contribute to lower S contents in apatite, and could also explain the exsolved Fe sulfide needles observed in at least one apatite core (Fig. 6).

In addition to the Fe sulfide needles, needles of Fe oxide are present in many of the apatite grains studied. The crystallographic orientation of these oxide needles also suggests that they exsolved from the host apatite, possibly in response to oxidation of Fe^{2+} in apatite. This process may have been contemporaneous with the subsolidus oxidation reactions elsewhere in the rock, such as pyrite $\rightarrow$ hydrous Fe-oxides + barite, and biotite $\rightarrow$ chlorite + hematite + rutile.

INTRACRYSTALLINE DIFFUSION

Among these apatite grains there is a correlation between the style of zoning and the sites occupied by the elements involved. Elements that substitute directly for Ca (i.e., Sr, Mn, Fe) show little or no zone-to-zone variation within a given crys-
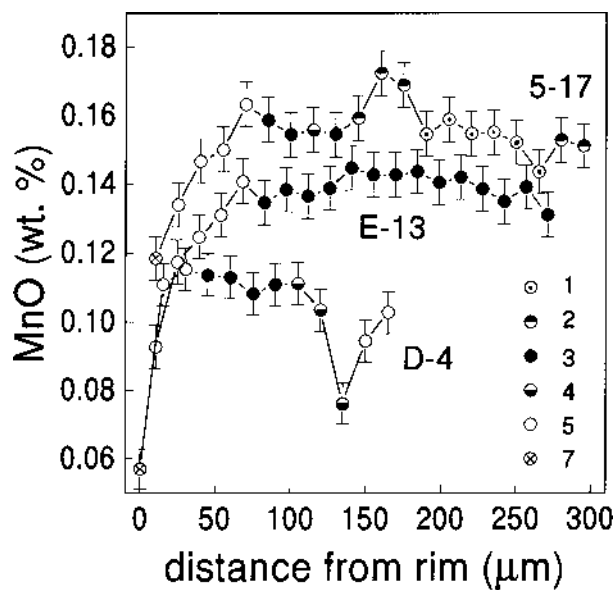
FIGURE 9. Comparison of MnO contents of apatite crystals 5-17, E-13, and D-4. Numbers indicate zones; error bars represent ±2σ analytical uncertainty based on counting statistics. Aside from a drop in concentration near the rims, there is limited MnO variation within individual crystals. However, grains that contain zones 1 or 2 (such as 5-17) tend to have higher MnO throughout, which we attribute to element redistribution (see text for discussion).
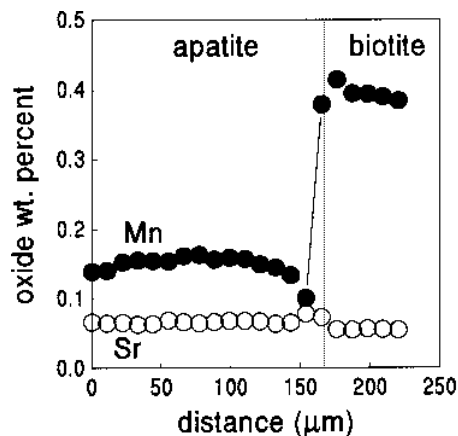

FIGURE 10. Variations in Mn and Sr content across an apatite-biotite grain boundary. Error bars representing 2σ analytical uncertainty (based on counting statistics) are smaller than the symbol size. Note the drop in Mn toward the apatite rim, and corresponding rise in Mn concentration toward the biotite rim, which is consistent with Mn exchange between these phases.

tal, but these elements may display significant differences in concentration between the same zone in different crystals. Conversely, elements that participate in coupled substitutions involving the tetrahedral site (i.e., Si, REE, Y, Na, S) show large zone-to-zone variations within an individual apatite, but these variations are similar in direction from one crystal to the next. In this section we present evidence that: (1) the lack of Mn, Fe, and Sr zoning reflects redistribution by intracrystalline diffusion; (2) REE patterns of individual zones were modified by intracrystalline diffusion; and (3) trace element variations that involve coupled substitutions with elements in the tetrahedral site preserve original magmatic zoning.

Zoning profiles for Sr are flat for all of the crystals studied (Fig. 3d), and there is no statistically significant difference in Sr content among any of the 16 apatite grains in which Sr was analyzed. This homogeneity could reflect a lack of primary magmatic zoning, but it is also possible that the Sr diffusion rate in apatite is sufficiently rapid that any original zoning was erased during slow cooling. Based on the diffusion data of Cherniak and Ryerson (1993), homogenization of Sr in a spherical apatite grain with a 100 μm radius would require only 14 000 years at 700 °C. There are no experimental data on Mn diffusion in apatite, but the rate should be similar to that of Sr, given the nearly identical site energy of the two cations [estimated from bond length and charge, after Dowty (1980)]. Similar to Sr, Mn zoning is flat across some crystals, but three significant aspects strongly suggest that the primary concentration gradients were homogenized by diffusion. First, some apatite grains display a subtle zone-to-zone variation, with higher

Mn in zones 1, 2, and/or 4 (Fig. 3). Second, the Mn content of an individual zone may differ by up to 50% from one apatite to the next (Fig. 9). Finally, Mn is generally higher in all zones of a given apatite if that grain contains zones 1 and/or 2, whereas Mn has a lower concentrations in all zones of those apatite grains that lack these early zones (Fig. 9). We believe the most likely explanation for this correlation is that Mn has been redistributed by diffusion, resulting in higher Mn throughout those crystals that initially contained Mn-rich zones 1 and/or 2, and lower Mn throughout apatites that lack these early zones. The alternative explanation, in which grain-to-grain Mn concentration variations are attributed to melt heterogeneity, would require the existence of many end-member liquids with different Mn and REE contents.

Over half of the apatite grains analyzed also show a 25–35% decrease in Mn content over the outer ~60 μm of the crystal (Figs. 3 and 9). This decrease does not correspond to a recognizable zone boundary, nor can it be attributed to analytical edge effects. Because previous studies have documented uptake of Sr from biotite by apatite during metamorphism (Wasserburg et al. 1964), a series of microprobe traverses were made across apatite-biotite, apatite-plagioclase, and apatite-quartz boundaries to determine whether the Mn drop might reflect an exchange process $Mn_{(apa)} \leftrightarrow Sr_{(bio)}$. Consistent with such an exchange, apatite grains adjacent to biotite show a drop in Mn toward the rim, accompanied in one case by a complementary rise in Mn within the biotite rim (Fig. 10). No such decrease was measured at the apatite-quartz boundary, however, an unexpected decrease in Mn was observed adjacent to plagioclase in one traverse. This observation would appear to require an alternative explanation, and perhaps reflects the influence of a phase that was out of the plane of the thin section.

For elements that participate in coupled substitutions in-

volving the tetrahedral site, slower diffusion rates are predicted on the basis of site energy estimates (Dowty 1980) and experimental studies of REE diffusion (Cherniak and Ryerson 1991; Cherniak 1997). Consistent with these predictions, abrupt concentration gradients in Si, REE, and Y at zone boundaries (Fig. 3) indicate that these elements have not been redistributed. However, ion microprobe data suggest that although original zone-to-zone variations in total REE content (ΣREE) are preserved, the original REE patterns of individual zones have been modified by intracrystalline diffusion. This modification is evident in La/Sm values, which vary significantly from one apatite to the next but display minimal variation within an individual crystal (Fig. 4). (In 11 of 13 apatites analyzed, zone-to-zone variation in La/Sm is within 2σ analytical uncertainty of the mean for the grain.) As with Mn, there is a crude correlation between higher La/Sm and the presence of zones 1 and/or 2 (Figs. 4 and 5a). The average $(La/Sm)_N$ for the nine grains that contain zones 1 and/or 2 is 0.30 ± 0.04 (1σ, compared to 0.22 ± 0.03 (1σ) for the four grains that lack these early zones. Because LREE preferentially occupy the Ca(2) site, homogenization of La/Sm requires only an exchange of REE on that site, and would be expected to proceed more rapidly than coupled exchanges that also involve the Ca(1) site or the tetrahedral site. Thus, we attribute the lack of zone-to-zone La/Sm variation and the correlation between higher La/Sm and the presence of zones 1 and/or 2 to REE redistribution: apatites that originally contained high La/Sm cores now have elevated La/Sm throughout (Fig. 4, grain E-3) whereas grains that lacked such cores now have lower La/Sm throughout (Fig. 4, grain B-5).

In contrast to La/Sm, homogenization of La/Yb involves an exchange of REE that favor different Ca sites. Raising La/Yb of an individual zone (while maintaining a fixed ΣREE content) would require some La (and other LREE) cations, which prefer Ca(2), to occupy sites filled previously by Yb (and other HREE), which prefer Ca(1). The unfavorable energetics of such an exchange may explain why many apatite grains in 91MT-68 retain core-to-rim La/Yb zoning (Fig. 5b) despite evidence for LREE mobility.

Any change in the ΣREE concentration of a zone would require a complementary redistribution of Si (or Na) between zones to maintain local charge balance. The diffusion rate of Si in apatite is expected to be low because of its high site energy [calculated after Dowty (1980)], and Si mobility may be the rate limiting process for REE diffusion in these grains. This effect has been noted by Cherniak (1997), who observed that REE diffusion rates measured in silica-bearing apatites (where the exchange mechanism is $REE^{3+} + Si^{4+} \leftrightarrow Ca^{2+} + P^{5+}$) are an order of magnitude slower than those measured in experiments with natural fluorapatite (where Sm diffusion involved either direct exchange of one REE for another, or the coupled exchange $REE^{3+} + Na^+ \leftrightarrow 2 Ca^{2+}$). An important implication of REE interdiffusion (La $\leftrightarrow$ Sm) being more rapid than ΣREE chemical diffusion is that relative and absolute REE abundances can be decoupled during diffusion, leading to a change in the REE pattern of a zone even though its ΣREE content remains the same.

Diffusion of sulfur in apatite is predicted to be very slow on the basis of site energy estimates for the S^{6+} ion (Dowty 1980).

However, despite greater analytical uncertainty for S than for REE or Si, it appears that in some grains S zonation is gradational over zones 1–3 (Fig. 3c and 3j). This suggests that S diffusion is more rapid than Si, and may indicate that S diffusion is influenced by changes in oxidation state. In the S^{4+} state, for example, S would have a slightly smaller ionic radius than Si^{4+} and might diffuse more rapidly. Alternatively, gradational zoning in S could be a primary magmatic trend.

IMPLICATIONS

Our conclusion that zoning in apatite records melt heterogeneity implies that such heterogeneity existed on the length scale represented by our rock sample (tens of centimeters), and/or that movement of crystals relative to one another within the magma occurred over sufficient distances that apatites growing in compositionally distinct parts of the magma could assemble within the volume represented by a ~10 kg sample. Movement of crystals would have become more restricted as crystallization of the host magma progressed, and would explain why later-formed apatite zones are less heterogeneous than the early zones. Establishment of a crystal framework that would prevent any further movement of crystals may be indicted by zone 5, the first one that is observed in all grains and shows no evidence of resorption. Delicate oscillations within this zone further imply slow crystallization under static conditions (Allegre et al. 1981).

Relative diffusion rates inferred from this study are consistent with predictions based on charge and bond length: Mn, Sr, Fe, and LaSm$_{-1}$ are faster than S and LaYb$_{-1}$, which are faster than Si. Na diffusion appears to be slower than expected, and is probably limited by the rate of S diffusion. Elements of particular interest for future diffusion experiments are Mn, Si, and REE. However, application of experimental data to natural systems will require knowledge of the particular substitution mechanisms involved, because rates for elements involved in coupled substitutions, such as the REE, may vary by an order of magnitude or more depending upon what other elements are involved.

The observation that intracrystalline diffusion rates vary from element to element has several important implications for petrologic interpretation of apatite zoning: (1) trace element and isotopic systematics of inherited cores (or other zones) may be disturbed, even in cases when zone boundaries appear sharp in BSE images. This is of particular concern for rapidly redistributed elements (Sr, Pb) in apatite grains where the only observed zoning profiles involve tetrahedral site elements. However, in cases where Sr zoning is present, other elements are likely to retain their magmatic distributions; (2) because REE interdiffusion [e.g., LaSm$_{-1}$ on the Ca(2) site] appears to occur more rapidly than redistribution of ΣREE (which requires a corresponding redistribution of Si), REE concentrations and REE patterns can be decoupled. Preservation of ΣREE zoning within an apatite does not therefore constitute evidence that primary variations in REE pattern, or Sm-Nd isotopic systematics, have been undisturbed. This could explain, for example, why Paterson et al. (1992) found Sm-Nd isotopic evidence of inheritance in zircon from the Strontian pluton, but not in apatite, despite the fact that both minerals contain rounded cores;

(3) sulfur occupies the tetrahedral site and appears to diffuse slowly, suggesting that S zoning in apatite may retain information about the f_{O_2} and/or vapor saturation history of a magma.

As the host for a diverse group of trace elements that diffuse at different rates, apatite has great potential as a tool for investigating the time-temperature history of crustal melting events (Watson and Harrison 1984). In the present case, we cannot place tight constraints on the thermal history of sample 91MT-68 because no diffusion-based chemical gradients were preserved for elements with known diffusion rates (Sr, REE). However, the abrupt changes in REE content across zone boundaries, which limit diffusion length to <5 mm, require sample 91MT-68 to have cooled below 600 °C in 10^6 year or less (based on data of Cherniak 1997). Extrapolation of such conclusions to a larger area (e.g., entire pluton) would require data from additional samples, but study of trace element zoning in apatite clearly has the potential to provide insights into the chemical and thermal history of igneous systems.

REFERENCES CITED

Allegre, C.J., Provost, A., and Jaupart, C. (1981) Oscillatory zoning: a pathological case of crystal growth. Nature, 294, 223–228.
Bacon, C.R. (1989) Crystallization of accessory phases in magmas by local saturation adjacent to phenocrysts. Geochimica et Cosmochimica Acta, 53, 1055–1066.
Baker, L.L. and Rutherford, M.J. (1996) Crystallization of anhydrite-bearing magmas. Transactions of the Royal Society of Edinburgh: Earth Sciences, 87, 243–250.
Bea, F., Pereira, M., and Stroh, A. (1994) Mineral/leucosome trace-element partitioning in a peraluminous migmatite (a laser ablation-ICP-MS study). Chemical Geology, 117, 291–312.
Bernard, A., Demaiffe, D., Mattielli, N., and Punongbayan, R. (1991) Anhydrite-bearing pumices from Mount Pinatubo: further evidence for the existence of sulfur-rich silicic magmas. Nature, 354, 139–140.
Boudreau, A.E., Mathez, E.A., and McCallum, I.S. (1986) Halogen geochemistry of the Stillwater and Bushveld complexes: evidence for transport of the platinum-group elements by Cl-rich fluids. Journal of Petrology, 27, 967–986.
Boynton, W.V. (1984) Cosmochemistry of the rare earth elements: meteorite studies. In P. Henderson, Ed., Rare earth element geochemistry, p. 63–114. Elsevier, Amsterdam.
Carroll, M.R. and Rutherford, M.J. (1987) The stability of igneous anhydrite: experimental results and implications for sulfur behavior in the 1982 El Chichon trachyandesite and other evolved magmas. Journal of Petrology, 28, 781–801.
Cherniak, D.J. (1997) Rare earth diffusion in fluorapatite. Eos, 78, 835–836.
Cherniak, D.J. and Ryerson, F.J. (1991) Diffusion of Sr and Sm in apatite. Eos, 72, 309.
——(1993) A study of strontium diffusion in apatite using Rutherford backscattering spectroscopy and ion implantation. Geochimica et Cosmochimica Acta, 57, 4653–4662.
Cherniak, D.J., Lanford, W.A., and Ryerson, F.J. (1991) Lead diffusion in apatite and zircon using ion implantation and Rutherford backscattering techniques. Geochimica et Cosmochimica Acta, 55, 1663–1673.
Czamanske, G.K., Ishihara, S., and Atkin, S.A. (1981) Chemistry of rock-forming minerals of the Cretaceous-Paleocene Batholith in southwestern Japan and implications for magma genesis. Journal of Geophysical Research, 86, 10431–10469.
Dowty, E. (1980) Crystal-chemical factors affecting the mobility of ions in minerals. American Mineralogist, 65, 174–182.
Fleck, R.J. (1990) Nd, Sr, and trace element evidence of crustal anatexis and magma mixing in the Idaho batholith. In R.L. Anderson, Ed., The nature and origin of Cordilleran magmatism: Geological Society of America Memoir, 174, 359–374.
Fleck, R.J. and Criss, R.E. (1985) Strontium and oxygen isotopic variations in Mesozoic and Tertiary plutons of central Idaho. Contributions to Mineralogy and Petrology, 90, 291–308.
Frost, B.R. (1991) Introduction to oxygen fugacity and its petrologic importance. In

Mineralogical Society of America Reviews in Mineralogy, 25, 1–9.
Gromet, L.P. and Silver, L.T. (1983) Rare earth element distributions among minerals in a granodiorite and their petrogenetic implications. Geochimica et Cosmochimica Acta, 47, 925–939.
Gunow, A.J. (1983) Trace element mineralogy in the porphyry molybdenum environment, 400 p. PhD. thesis, University of Colorado, Boulder, Colorado.
Harrison, T.M. and Watson, E.B. (1984) The behavior of apatite during crustal anatexis: equilibrium and kinetic considerations. Geochimica et Cosmochimica Acta, 48, 1467–1477.
Hughes, J.M., Cameron, M., and Crowley, K.D. (1991a) Ordering of divalent cations in the apatite structure: crystal structure refinements of natural Mn- and Sr-bearing apatite. American Mineralogist, 76, 1857–1862.
Hughes, J.M., Cameron, M., and Mariano, A.N. (1991b) Rare-earth-element ordering and structural variations in natural rare-earth-bearing apatites. American Mineralogist, 76, 1165–1173.
Jolliff, B.L., Papike, J.J., and Shearer, C.K. (1989) Inter- and intra-crystal REE variations in apatite from the Bob Ingersoll pegmatite, Black Hills, South Dakota. Geochimica et Cosmochimica Acta, 53, 429–441.
Knutson, C., Peacor, D.R., and Kelly, W.C. (1985) Luminescence, color and fission track zoning in apatite crystals of the Panasqueira tin-tungsten deposit, Beira-Baixa, Portugal. American Mineralogist, 70, 829–837.
Kouchi, A., Sugawara, Y., Kashima, K., and Sunagawa, I. (1983) Laboratory growth of sector zoned clinopyroxenes in the system CaMgSi$_2$O$_6$-CaTiAl$_2$O$_6$. Contributions to Mineralogy and Petrology, 83, 177–184.
Kuehner, S.M. and Joswiak, D.J. (1996) Naturally occurring ferric iron sanidine from the Leucite Hills lamproite. American Mineralogist, 81, 229–237.
Lewis, R.S., Burmeister, R.F., Reynolds, R.W., Bennett, E.H., Myers, P.E., and Reid, R.R. (1992) Geologic Map of the Lochsa River Area, Northern Idaho. Idaho Geologic Survey Press, Geologic Map Series.
Luhr, J.F. (1990) Experimental phase relations of water- and sulfur-saturated arc magmas and the 1982 eruptions of El Chichon volcano. Journal of Petrology, 31, 1071–1114.
Luhr, J.F., Carmichael, I.S.E., and Varekamp, J.C. (1984) The 1982 eruptions of El Chichon volcano, Chiapas, Mexico: mineralogy and petrology of anhydrite bearing pumices. Journal of Volcanology and Geothermal Research, 23, 69–108.
Mahood, G. and Hildreth, W. (1983) Large partition coefficients for trace elements in high-silica rhyolites. Geochimica et Cosmochimica Acta, 47, 11–30.
Montel, J. (1993) A model for monazite/melt equilibrium and application to the generation of granitic magmas. Chemical Geology, 110, 127–146.
Mueller, P.A., Shuster, R.D., D'Arcy, K.A., Heatherington, A.L., Nutman, A.P., and Williams, I.S. (1995) Source of the northeastern Idaho batholith: isotopic evidence for a Paleoproterozoic terrane in the northwestern U.S. Journal of Geology, 103, 63–72.
O'Brien, H.E., Irving, A.J., and McCallum, I.S. (1988) Complex zoning and resorption of phenocrysts in mixed potassic mafic magmas of the Highwood Mountains, Montana. American Mineralogist, 73, 1007–1024.
Paterson, B.A. and Stephens, W.E. (1992) Kinetically induced compositional zoning in titanite: implications for accessory-phase/melt partitioning of trace elements. Contributions to Mineralogy and Petrology, 109, 373–385.
Paterson, B.A., Rogers, G., and Stephens, W.E. (1992) Evidence for inherited Sm-Nd isotopes in granitoid zircons. Contributions to Mineralogy and Petrology, 111, 378–390.
Pichavant, M., Montel, J., and Richard, L.R. (1992) Apatite solubility in peraluminous liquids: experimental data and an extension of the Harrison-Watson model. Geochimica et Cosmochimica Acta, 56, 3855–3861.
Rakovan, J. and Reeder, R.J. (1994) Differential incorporation of trace elements and dissymmetrization in apatite: the role of surface structure during growth. American Mineralogist, 79, 892–903.
Ronsbo, J.G. (1989) Coupled substitutions involving REEs and Na and Si in apatites in alkaline rocks from the Ilimaussaq intrusion, South Greenland, and the petrological implications. American Mineralogist, 74, 896–901.
Sakuyama, M. (1979) Evidence of magma mixing: petrological study of Shirouma-Oike calc-alkaline andesite volcano, Japan. Journal of Volcanology and Geothermal Research, 5, 179–208.
Sawka, W.N. (1988) REE and trace element variations in accessory minerals and hornblende from the strongly zoned McMurry Meadows pluton, California. Transactions of the Royal Society of Edinburgh: Earth Sciences, 79, 157–168.
Shuster, R.D. and Bickford, M.E. (1985) Chemical and isotopic evidence for the petrogenesis of the northeastern Idaho batholith. Journal of Geology, 93, 727–742.
Toth, M. and Stacey, J.S. (1992) Constraints on the formation of the Bitterroot lobe of the Idaho batholith, Idaho and Montana, from U-Pb zircon geochronology and feldspar Pb isotopic data. U.S. Geological Survey Bulletin, 2008, 14 p.
Wasserburg, G.J., Albee, A.L., and Lanphere, M.A. (1964) Migration of radiogenic strontium during metamorphism. Journal of Geophysical Research, 69, 4395–4401.
Watson, E.B. and Green, T.H. (1981) Apatite/liquid partition coefficients for the rare earth elements and strontium. Earth and Planetary Science Letters, 56, 405–421.
Watson, E.B. and Harrison, T.M. (1983) Zircon saturation revisited: temperature and composition effects in a variety of crustal magma types. Earth and Planetary

Science Letters, 64, 295–304.
——— (1984) Accessory minerals and the geochemical evolution of crustal magmatic systems: a summary and prospectus of experimental approaches. Physics of the Earth and Planetary Interiors, 35, 19–30.
Watson, E.B., Harrison, T.M., and Ryerson, F.J. (1985) Diffusion of Sm, Sr, and Pb in fluorapatite. Geochimica et Cosmochimica Acta, 49, 1813–1823.
Wiswall, C.G. and Hyndman, D.W. (1987) Emplacement of the main plutons of the Bitterroot lobe of the Idaho batholith. In T.L. Vallier and H.C. Brooks, Eds. Geology of the Blue Mountains region of Oregon, Idaho, and Washington: the Idaho batholith and its border zone. U.S. Geological Survey Professional Paper 1436, 59–71.

Wolf, M.B. and London, D. (1994) Apatite dissolution into peraluminous haplogranitic melts: an experimental study of solubilities and mechanisms. Geochimica et Cosmochimica Acta, 58, 4127–4145.
Wones, D.R. and Eugster, H.P. (1965) Stability of biotite: experiment, theory, and application. American Mineralogist, 50, 1228–1272.
Ziebold, T.O. (1967) Precision and sensitivity in electron microprobe analysis. Analytical Chemistry, 39, 858–861.